

Quantized charge fractionalization at quantum Hall Y junctions in the disorder dominated regime

Chaojing Lin^{1,2✉}, Masayuki Hashisaka³, Takafumi Akiho³, Koji Muraki³ & Toshimasa Fujisawa^{1✉}

Fractionalization is a phenomenon where an elementary excitation partitions into several pieces. This picture explains non-trivial transport through a junction of one-dimensional edge channels defined by topologically distinct quantum Hall states, for example, a hole-conjugate state at Landau-level filling factor $\nu = 2/3$. Here we employ a time-resolved scheme to identify an elementary fractionalization process; injection of charge q from a non-interaction region into an interacting and scattering region of one-dimensional channels results in the formation of a collective excitation with charge $(1-r)q$ by reflecting fractionalized charge rq . The fractionalization factors, $r = 0.34 \pm 0.03$ for $\nu = 2/3$ and $r = 0.49 \pm 0.03$ for $\nu = 2$, are consistent with the quantized values of $1/3$ and $1/2$, respectively, which are expected in the disorder dominated regime. The scheme can be used for generating and transporting fractionalized charges with a well-defined time course along a well-defined path.

¹Department of Physics, Tokyo Institute of Technology, 2-12-1 Ookayama, Meguro, Tokyo 152-8551, Japan. ²Tokyo Tech Academy for Super Smart Society, Tokyo Institute of Technology, 2-12-1 Ookayama, Meguro, Tokyo 152-8551, Japan. ³NTT Basic Research Laboratories, NTT Corporation, 3-1 Morinosato-Wakamiya, Atsugi, Kanagawa 243-0198, Japan. ✉email: lin.c.ad@m.titech.ac.jp; fujisawa@phys.titech.ac.jp

One-dimensional electronic systems provide non-trivial many-body effects that cannot be explained with single-particle pictures¹. Theoretically, these effects can be calculated using bosonization techniques and the bosonic (plasmonic) scattering approach, which have been applied for both dc and ac responses even in inhomogeneous and disordered systems^{1–6}. Experimentally, many-body states can be investigated using electronic and optical techniques^{7–10}. Among them, one-dimensional edge channels in integer and fractional quantum Hall (QH) systems^{11–14} are attractive for studying non-trivial excitations in multiple channels by utilizing mesoscopic devices^{15–18}. The focus of this study is transport eigenmodes that govern the interacting edge channels.

For example, the charge and spin (dipolar) modes for copropagating channels in the integer QH system at $\nu = 2$ were investigated based on the Coulomb interaction in terms of the chiral Tomonaga-Luttinger liquid^{19–21}. At a Y-junction where two decoupled channels join to form an interacting region, an electronic excitation incident from the non-interacting region is fractionalized into non-trivial charge and spin excitations in the interacting region^{19,22–24}. In the absence of interchannel tunneling, the eigenmodes are determined by the interaction parameters and can hence deviate from the pure charge and spin modes. In this interaction-dominated regime, the fractionalization ratio assumes a non-universal interaction-dependent value, as demonstrated in frequency- and time-resolved measurements as well as noise measurements^{25–27}.

A similar class of coupled modes appears when disorder allows for significant tunneling between two edge channels. A well-known example is the charge and neutral modes in the ‘hole conjugate’ fractional QH state at $\nu = 2/3$, as suggested by noise measurements and transport properties for short interacting regions^{28–33}. We assumed a reconstructed edge with counterpropagating integer and fractional channels^{12,13}, whereas alternative effective models can be considered^{34,35}. Theoretically, the charge and neutral modes appear at the Kane-Fisher-Polchinski fixed point in the renormalization group flow³⁶. In this disorder-dominated regime, an elementary excitation should be fractionalized into pure charge and neutral modes with a quantized ratio at a Y junction of interacting and non-interacting regions^{36,37}.

In this study, we have experimentally identified this quantized fractionalization ratio by employing time-resolved measurements for the hole-conjugate fractional state at $\nu = 2/3$. A similar quantized fractionalization is also found in the integer QH state at $\nu = 2$ in the presence of significant tunneling. The obtained feature is supported by a simulation involving a realistic model based on the plasmon scattering approach. The quantized charge fractionalization describes the dc characteristics as well.

Results

Fractionalization processes. We first consider the edge of the fractional state at $\nu = 2/3$, where the counterpropagating $\Delta\nu = 1$ and $1/3$ one-dimensional channels¹² are formed along the interface to the electronic vacuum ($\nu = 0$), as shown in Fig. 1a. Here, $\Delta\nu = |\nu_1 - \nu_2|$ denotes a channel along an interface between insulating (incompressible) regions with $\nu = \nu_1$ and ν_2 . Disorder-induced scattering renders them describable as a composite $\Delta\nu = 2/3$ channel with two counterpropagating transport modes³⁶, i.e., a charge mode carrying a charge and a neutral mode carrying heat. We address fractionalization processes at Y-junctions comprising $\Delta\nu = 1$, $2/3$, and $1/3$ channels, as shown in Fig. 1b–d. Two types of Y-junctions are possible, i.e., Y_C and Y_N , which form depending on the cyclic order of the insulating regions and the direction of the magnetic field B . For the configuration shown in Fig. 1b, a wave packet of charge q incident

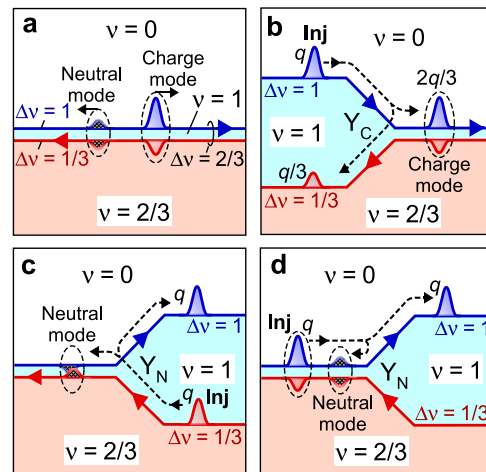


Fig. 1 QH Y-junctions formed with $\Delta\nu = 1$, $2/3$, and $1/3$ channels. **a** The charge and neutral modes in the disorder dominated regime of a composite $\Delta\nu = 2/3$ channel comprising $\Delta\nu = 1$ (blue) and $1/3$ (red) channels along the boundaries of a hole-conjugate QH region with $\nu = 2/3$, a narrow integer state with $\nu = 1$, and the electronic vacuum ($\nu = 0$). Excitations are represented by positive and negative wave packets with ratios of charges in $\Delta\nu = 1$ and $1/3$ channels ($1:-1/3$ for the charge mode and $1:-1$ for the neutral mode). **b** Charge fractionalization at junction Y_C . An incoming wave packet with charge q in the $\Delta\nu = 1$ channel is fractionalized into two packets with $2q/3$ (comprising q and $-q/3$) in the $\Delta\nu = 2/3$ channel and $q/3$ in the $\Delta\nu = 1/3$ channel. **c**, **d** Neutral reflections at junction Y_N . An injected packet with charge q in the $\Delta\nu = 1/3$ channel splits into charge q in the $\Delta\nu = 1$ channel and neutral excitation (comprising $-q$ and q) in the $\Delta\nu = 2/3$ channel in **c**, and so as the packet in the $\Delta\nu = 2/3$ channel in **d**.

from the $\Delta\nu = 1$ channel is fractionalized with factor r ($= 1/3$ in the disorder dominated regime) at junction Y_C into fractional charges $(1-r)q$ and rq , which propagate through the $\Delta\nu = 2/3$ and $\Delta\nu = 1/3$ channels, respectively. This occurs because the charge mode in the $\Delta\nu = 2/3$ channel is composed of charges q in the $\Delta\nu = 1$ channel and $-rq$ in the $\Delta\nu = 1/3$ channel³⁶. The formation of this collective excitation requires a charge rq to be reflected back into the uncoupled $\Delta\nu = 1/3$ channel³⁷. A similar reflection is expected when a wave packet of charge q is injected from a $\Delta\nu = 1/3$ channel to junction Y_N shown in Fig. 1c, where neutral excitation in the $\Delta\nu = 2/3$ channel is formed by reflecting charge q in the downstream $\Delta\nu = 1$ channel. As shown in Fig. 1d, a charge wave packet in the charge mode of the $\Delta\nu = 2/3$ channel is decomposed into a charge in the $\Delta\nu = 1$ channel and heat in the neutral mode. We focus on the charge fractionalization by neglecting neutral excitations as the length of the $\Delta\nu = 2/3$ channel ($L > 100 \mu\text{m}$) is much longer than the equilibration length l_{eq} (typically $\sim 10 \mu\text{m}$)^{32,33}.

Quantized fractionalization in $\nu = 2/3$ case. We demonstrate the charge fractionalization in time-domain measurements using several devices formed in a standard AlGaAs/GaAs heterostructure (see Methods and Supplementary Note 1). The following data were obtained at ~ 50 mK from devices #1 and #2 fabricated on the same chip, as schematically shown in Fig. 2a. For device #1, two Y-junctions, Y_C and Y_N , formed at the intersections of the three regions—the ungated region with bulk filling factor $\nu_B = 2/3$, the gated region with a tunable ν_G ($= 1$ in Fig. 2a), and vacuum. An initial charge wave packet was excited by applying a voltage step to the injector gate G_I , and the waveforms of the charge packets after passing through the junctions were investigated by applying a voltage pulse of width t_w (0.08–0.15 ns) to the detector gate G_D . Charge waveforms were

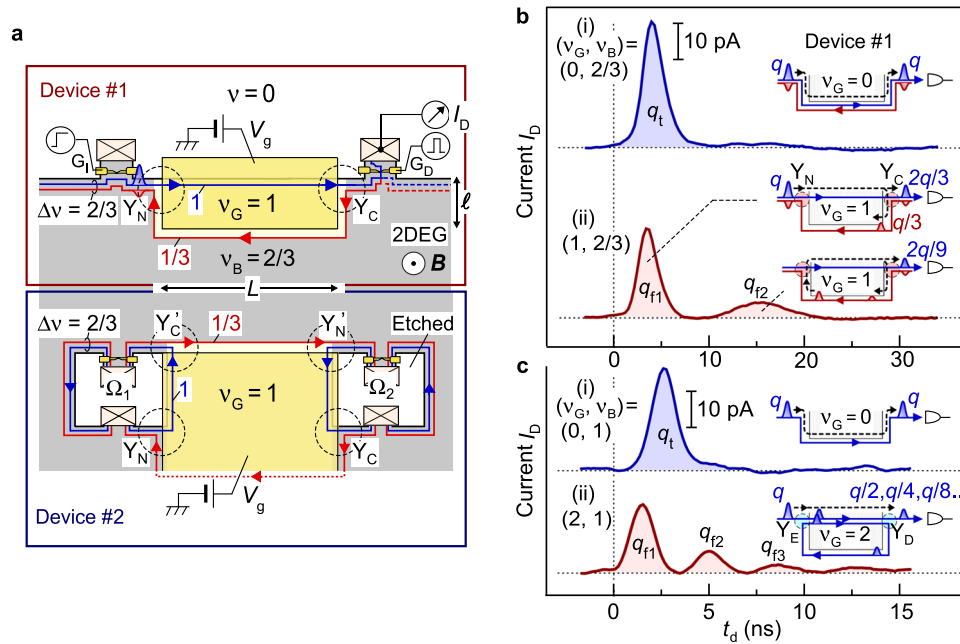


Fig. 2 Quantized fractionalization of charge wave packets. **a** Measurement setup with devices #1 and #2. Application of voltage V_g to the large gate (yellow) forms a rectangular QH region ($L = 300 \mu\text{m}$ and $l = 20 \mu\text{m}$ for #1) and QH junctions Y_N and Y_C at $\nu_G = 1$ and $\nu_B = 2/3$. For #1, an initial wave packet is excited by applying a voltage step to the injector gate G_1 with the underneath fully depleted. Fractionalized wave packets are detected by applying a voltage pulse of width t_w to transmit a part of the packet to be detected as current I_D . For #2, two-terminal dc conductance G through similar Y-junctions is measured with ohmic contacts in Corbino geometry. **b** Typical charge waveforms obtained in current I_D as a function of delay time t_d of the detector voltage pulse with respect to the excitation voltage step. The reference trace (i) at $\nu_G = 0$ ($V_g = -0.3 \text{ V}$) and trace (ii) showing charge fractionalizations at $\nu_G = 1$ ($V_g = 0.26 \text{ V}$) were obtained at $\nu_B = 2/3$ ($B = 11.5 \text{ T}$). Areas under the peaks represent charges with ratios $q_{f1}/q_t \sim 2/3$ and $q_{f2}/q_{f1} \sim 2/9$. **c** The reference trace (i) at $\nu_G = 0$ ($V_g = -0.3 \text{ V}$) and trace (ii) showing fractionalizations at $\nu_G = 2$ ($V_g = 0.34 \text{ V}$) obtained at $\nu_B = 1$ ($B = 7.5 \text{ T}$). The areas under the peaks show $q_{f2}/q_{f1} \sim 1/2$ and $q_{f3}/q_t \sim 1/4$. Propagation of charge wave packets is illustrated in the respective insets.

obtained by measuring the detector current I_D at various time delays t_d of the voltage pulse with respect to the voltage step (see Methods)³⁸. Trace (i) in Fig. 2b is a reference showing that a single charge packet was observed for $\nu_G = 0$ (the gate voltage $V_g = -0.3 \text{ V}$), i.e., when a single $\Delta\nu = 2/3$ channel without Y-junctions is formed, as shown in the inset. This is a typical characteristic of the edge magnetoplasmon mode^{39–41} at $\nu = 2/3$. When the Y_C and Y_N junctions were activated by setting $\nu_G = 1$ ($V_g = +0.26 \text{ V}$, $B = 11.5 \text{ T}$), a clear charge fractionalization manifested as two distinct packets in trace (ii). The first packet is associated with the direct propagation through junction Y_N , $\Delta\nu = 1$ channel, and junction Y_C . The second one is delayed by the round trip around the gated region, as illustrated in the insets. Subsequent packets associated with further fractionalization processes are extremely small to be resolved. By assuming $r = 1/3$, the entire process yields a series of packets with $2q/3, 2q/9, \dots$ toward the detector. We evaluated the charge q_t in the reference wave packet in (i) as well as q_{f1} and q_{f2} in the first and second packets in (ii), respectively, from the area of the peaks. The obtained q_t, q_{f1} , and q_{f2} are plotted in Fig. 3b as a function of V_g , with the vertical axis normalized by the q_t value at $V_g = -0.3 \text{ V}$ ($\nu_G = 0$). The ratios q_{f1}/q_t and q_{f2}/q_t are similar to the expected values of $(1-r) = 2/3$ and $(1-r)r = 2/9$, respectively, when the $\Delta\nu = 1$ and $1/3$ channels are well defined at $\nu_G \geq 1$. In particular, $r = q_{f2}/q_{f1}$ estimated from each I_D profile yields $r = 0.34 \pm 0.03$ in the range of $V_g = 0.21\text{--}0.27 \text{ V}$, as shown in the inset of Fig. 3b, consistent with the quantized value of $1/3$.

This observation is supported by the dc characteristics of device #2, which has Corbino geometry with ohmic contacts surrounded by a QH state, as shown in the lower part of Fig. 2a. Transport through the $\Delta\nu = 1/3$ channel formed between $\nu_G = 1$ and $\nu_B = 2/3$ regions involves the equilibration associated with scattering between the coupled $\Delta\nu = 1$ and $1/3$ channels inside

the composite $\Delta\nu = 2/3$ channels. Fig. 3a shows the two-terminal conductance G between ohmic contacts Ω_1 and Ω_2 with other ohmic contacts floating. The clear plateau of $G \cong e^2/6h$ at $V_g \sim +0.2 \text{ V}$ ($\nu_G = 1$) ensures a full equilibration in the $\Delta\nu = 1/3$ channel and negligible backscattering in both $\nu_G = 1$ and $\nu_B = 2/3$ regions. This is a requisite for clear quantization of $r = 1/3$. Whereas the dc characteristics of systems involving composite $\Delta\nu = 2/3$ channels have been successfully explained in various ways^{32,33,37}, we herein demonstrate that the same can also be understood with the quantized charge fractionalization. As shown by the simplified channel configuration in the inset of Fig. 3a, a fictitious charge packet q emanating from Ω_1 is fractionalized into a series of charge packets through the paths shown by the dashed lines. Some of them reach Ω_2 with the first charge $2q/9$ through path $\Omega_1 - Y_N - Y_C' - Y_N' - Y_C - \Omega_2$, followed by others multiplied by the geometric ratio of $1/9$ associated with round trip $Y_C - Y_N - Y_C' - Y_N' - Y_C$. The total charge $q/4$ reaching Ω_2 explains $G = e^2/6h$ for the conductance $2e^2/3h$ of the source channels connected to Ω_1 and Ω_2 . Hence, charge fractionalization provides a unified view of dc and time-dependent charge transport.

Quantized fractionalization in $\nu = 2$ case. We observed similar quantized fractionalization with integer QH states at $\nu_G = 2$ and $\nu_B = 1$, when the two $\Delta\nu = 1$ channels with up- and down-spins were prepared in the disorder-dominated regime. The two channels are coupled to form a composite $\Delta\nu = 2$ channel, as shown in the bottom inset of Fig. 2c. Significant scattering between them is allowed for example by coupling to nuclear spins⁴². Separate experiments show full equilibration for a channel length of $\sim 300 \mu\text{m}$ in device #2 (see Supplementary Note 2). Our previous study showed a short equilibration length of $\sim 10 \mu\text{m}$ in a similar device with a slightly lower electron

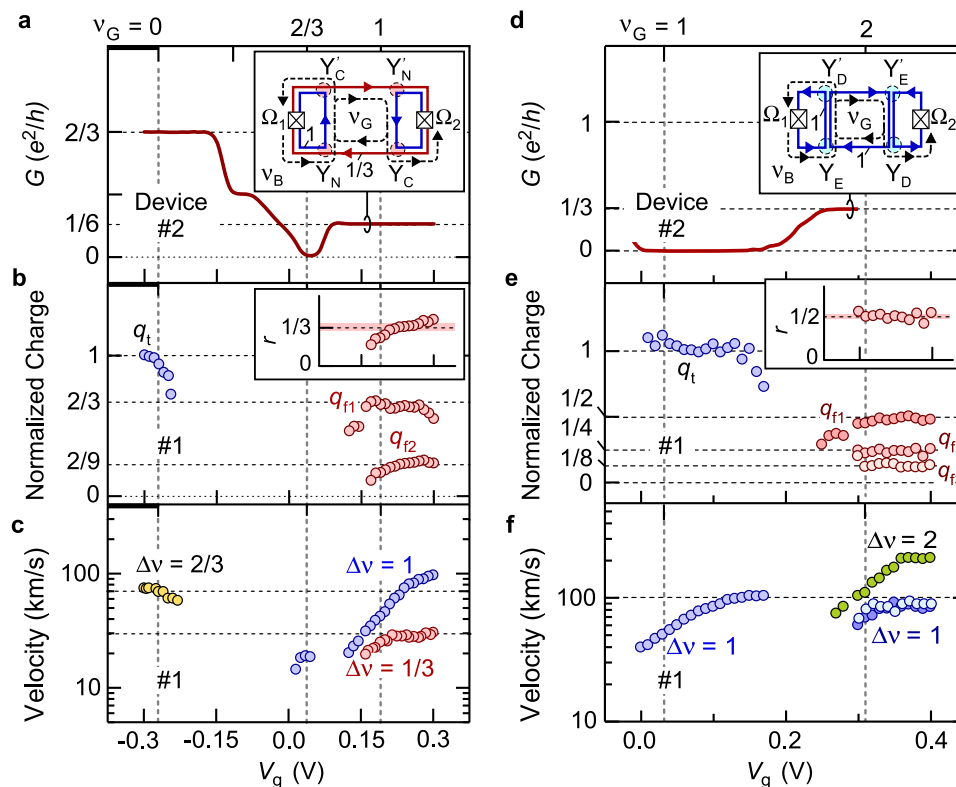


Fig. 3 Characteristics of charge transport. **a, d** V_g -dependence of two-terminal conductance G measured with ohmic contacts Ω_1 and Ω_2 of device #2 obtained at $\nu_B = 2/3$ in **a** and $\nu_B = 1$ in **d**. The insets show the channel configurations, where multiple charge fractionalizations at Y-junctions explain the plateau $G = e^2/6h$ at $\nu_G = 1$ in **a** and $G = e^2/3h$ at $\nu_G = 2$ in **d**. **b, e** The reference charge q_t , and fractionalized charges q_{f1} , q_{f2} , and q_{f3} in the respective packets normalized by q_t . A single reference packet typically involves $q_t \cong 240e$ in **b** and $30e$ in **e**. The clear plateaus of q_i/q_t indicate the quantized fractionalization. The insets show fractionalization factor $r = q_{f2}/q_{f1}$ with a constant region ($r = 0.34 \pm 0.03$ in **b** and $r = 0.49 \pm 0.03$ in **e**). **c, f** Charge velocities of the channels. The $\Delta\nu = 1/3$ interface channel between $\nu = 1$ and $2/3$ regions, the $\Delta\nu = 1$ edge channel between $\nu_G = 1$ and vacuum, and the $\Delta\nu = 2/3$ composite channel between $\nu_G = 0$ and $\nu_B = 2/3$ are shown in **c**, whereas the $\Delta\nu = 1$ interface channel between $\nu_G = 2$ and $\nu_B = 1$ regions ($0.3 \text{ V} < V_g < 0.4 \text{ V}$, estimated from the second and the third packets), the $\Delta\nu = 1$ edge channel between $\nu_G = 1$ and vacuum ($V_g < 0.18 \text{ V}$), and the $\Delta\nu = 2$ composite channel between $\nu_G = 2$ and vacuum are shown in **f**. Data in **b, c, e**, and **f** were obtained using device #1. Vertical dotted lines for representative ν_G values were determined from a separate four-terminal measurement (See Supplementary Note 1).

density³³. In this disorder-dominated regime, the transport eigenmodes of the $\Delta\nu = 2$ channel should be a pure symmetric charge mode and a short-lived antisymmetric neutral mode (see Methods). These modes are excited at junction Y_E and decomposed at junction Y_D with quantized charge fractionalization of factor $r = 1/2$. Namely, a single charge packet with q in the symmetric mode splits into two packets with $(1-r)q$ and rq in the up- and down-spin channels, respectively. Compared with the reference trace (i) in Fig. 2c for $(\nu_G, \nu_B) = (0, 1)$, trace (ii) shows charge fractionalizations for $(\nu_G, \nu_B) = (2, 1)$ at $V_g = +0.34 \text{ V}$ and $B = 7.5 \text{ T}$. A series of well-isolated packets, q_{f1}, q_{f2}, \dots , manifests the multiple fractionalization processes at Y_D . As plotted in Fig. 3e, the fractionalization factor $r = q_{f1}/q_{f2} = 0.49 \pm 0.03$ obtained in the range of $V_g = 0.31\text{--}0.37 \text{ V}$ is consistent with the quantized value of $1/2$. This is in contrast to previous studies pertaining to the interaction dominated regime, where asymmetric modes with an interaction dependent factor of $r \sim 0.4$ were observed^{26,27}.

We observed a clear two-terminal conductance plateau $G = e^2/3h$ at $(\nu_G, \nu_B) = (2, 1)$ using device #2, as shown in Fig. 3d. This conductance is $1/3$ of the original $G = e^2/h$ of the single integer channel emanating from the ohmic contacts. This can be understood as the sum of the first transmission coefficient (the square of the fractionalization factor $1/2$) of a fictitious charge packet through path $\Omega_1 - Y_E - Y_D' - Y_E' - Y_D - \Omega_2$ followed by others with a geometric ratio of $1/4$ associated with round trip $Y_D - Y_E - Y_D' - Y_E' - Y_D$, as

shown in the inset. Hence, the quantized fractionalization also explains the dc characteristics of the integer channels.

Plasmon velocities. The velocity of the wave packet is an important parameter that reflects the interaction, as evident from chiral Tomonaga-Luttinger theories^{2,10,19}. We experimentally estimated the velocities from the time of flight, as summarized in Fig. 3c, f. The velocities of the edge channels ($\Delta\nu = 1$ channel between $\nu_G = 1$ and vacuum and $\Delta\nu = 2/3$ channel between $\nu_G = 0$ and $\nu_B = 2/3$ in Fig. 3c) are comparable to those in previous reports regarding edge magnetoplasmons^{38,39,43,44}. The velocity of the $\Delta\nu = 1/3$ interface channel between the $\nu = 1$ and $2/3$ regions, $\sim 30 \text{ km/s}$, is particularly important for transporting fractional charges⁴⁵. Unlike edge channels with a well-defined confining potential, the interface channel is supported by two QH states with a slight difference in their electrostatic potentials. Therefore, the contribution of the single-particle drift velocity arising from the potential gradient is negligible. This is particularly relevant to the $\Delta\nu = 1/3$ channel, as the Fermi level remains in the lowest Landau level in the fractional state.

To understand the origin of the velocity, we assume that the charge velocity of a $\Delta\nu$ channel is expressed as $v_c = \Delta\nu g_q/C$, where $g_q = e^2/h$ is the quantized conductance, and $1/C$ measures the interaction¹⁶. Practically, C should be dominated by the geometric capacitance (per unit length) between the channel and a nearby gate⁴⁶. For an interface channel along the side of the gate shown in

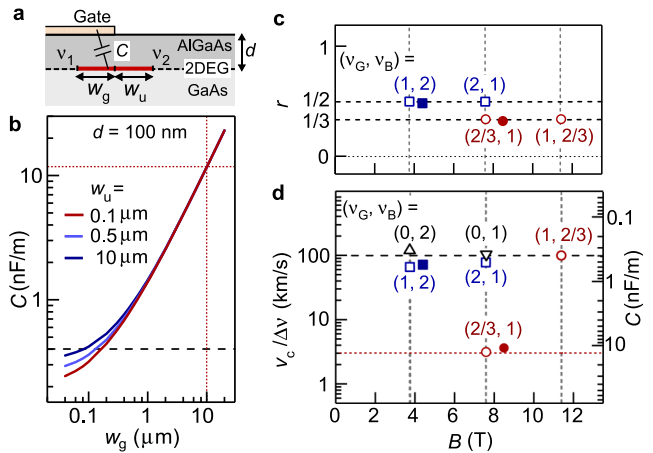


Fig. 4 Velocity of the interface mode. **a** Schematic cross-section around the interface channel $\Delta\nu = |\nu_1 - \nu_2|$ of width $w_g + w_u$ (w_g in the gated region and w_u in the ungated region) between two QH states at ν_1 and ν_2 . The interaction inside the channel can be described with geometric capacitance C to the gate. **b** Calculated capacitance C as a function of w_g for several w_u values. **c** Fractionalization factor r for junction Y_C obtained at $(\nu_G, \nu_B) = (2/3, 1)$ and $(1, 2/3)$ showing $r \sim 1/3$ (circles), and junction Y_D at $(1, 2)$ and $(2, 1)$ showing $r \sim 1/2$ (squares). **d** Normalized charge velocities $v_c/\Delta\nu$ for fractional $\Delta\nu = 1/3$ interface channels at $(2/3, 1)$ and $(1, 2/3)$ marked with circles, integer $\Delta\nu = 1$ interface channels at $(1, 2)$ and $(2, 1)$ marked with squares, and conventional edge channels at $(0, 2)$ and $(0, 1)$ marked with triangles. Data obtained after light irradiation are marked with solid symbols. Channel capacitance C is shown on the right scale.

Fig. 4a, this C is expected to depend on the width, $w = w_g + w_u$, of the channel (compressible region), where w_g (w_u) is the spread under the gate (in the ungated region). Our numerical simulation (see Methods) shows that C is determined primarily by w_g rather than w_u (Fig. 4b). The normalized velocities, $v_c/\Delta\nu$, obtained for various values of (ν_G, ν_B) , are summarized in Fig. 4d. Here, the data for $\nu_G > \nu_B$ and $\nu_G < \nu_B$ were obtained using devices #1 and #2, respectively, with $V_g > 0$ and $V_g < 0$ (see Supplementary Notes 2 and 3). Except for $(\nu_G, \nu_B) = (2/3, 1)$, $v_c/\Delta\nu$ indicates similar values for all interface channels, i.e. $\Delta\nu = 1/3$ (circles) and 1 (squares), as well as edge channel $\Delta\nu = 1$ (triangles). This coincidence suggests that the velocities are determined by a similar $C \sim 0.4$ nF/m, as shown on the right axis. A comparison with Fig. 4b implies that w_g is sufficiently narrow, comparable to the depth $d \sim 100$ nm of the electron system from the surface. This indicates that the velocity ~ 30 km/s of the $\Delta\nu = 1/3$ channel obtained for $(\nu_G, \nu_B) = (1, 2/3)$ is reasonable. Meanwhile, a significantly lower velocity of ~ 1 km/s was observed for the $\Delta\nu = 1/3$ channels in the $(2/3, 1)$ configuration. This suggests a wide $w_g \sim 10$ μm in the crude model or quasi-diffusive transport in the presence of disorder potential. Whereas this might be related to the small energy gaps of the QH states at lower B in this configuration, the velocity did not increase significantly with B even after light irradiation (solid circle), which increased the electron density. The former $(1, 2/3)$ configuration with a fractional state in an ungated region might be suitable for minimizing the time-of-flight and hence decoherence in a fractional-charge interferometer. It is noteworthy that the fractionalization factor r summarized in Fig. 4c remained at approximately $1/3$ even when the velocity reduced significantly.

Discussion

The observation above suggests robust fractionalization factors in the disorder-dominated regime. This is consistent with the plasmon (charge density wave) transport model (see Methods) shown in Fig. 5a, where interaction and scattering are characterized by

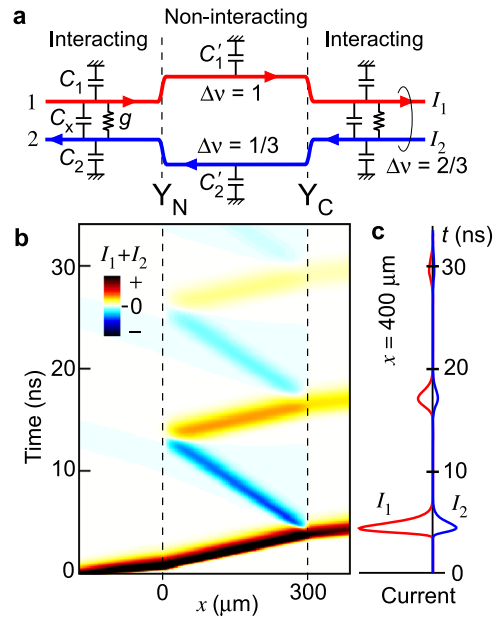


Fig. 5 Charge fractionalization calculated using a plasmon model. **a** Non-interacting edge channels $\Delta\nu = 1$ and $\Delta\nu = 1/3$ in the central region and composite $\Delta\nu = 2/3$ channels in the interaction regions on both sides, forming junctions Y_N and Y_C . **b** Time evolution of a charge wave packet initially prepared in the left interacting region at $x = -200$ μm , showing full transmission and full reflection at Y_N ($x = 0$) and charge fractionalization at Y_C ($x = 300$ μm). The sum of the currents I_1 and I_2 in the original $\Delta\nu = 1$ and $1/3$ channels, respectively, is plotted in a color scale (red for positive and blue for negative in an arbitrary unit). The numerical simulation was performed using realistic parameters: capacitances $C_1 = C_2 = C_x = 0.07$ nF/m; scattering conductance g inducing $l_{\text{eq}} = 10$ μm in the interacting regions; $C'_1 = C'_2 = 0.4$ nF/m in the non-interaction region. **c** Time-dependent I_1 and I_2 at $x = 400$ μm in right interaction region. Each packet shows $I_2 = -I_1/3$ of the charge mode.

distributed capacitances and scattering conductances, respectively^{46–48}. The transport eigenmodes generally deviate from the pure charge and neutral modes at higher frequencies. However, the deviation is small in the low-frequency regime, where the wavelength λ of the plasmon is much greater than the equilibration length l_{eq} . This is observed in the numerical simulation of multiple charge fractionalizations with realistic parameters, as shown in Fig. 5b, c, where the distortion of the charge waveform is negligible. The obtained narrow width (a few nanoseconds) of the fractionalized wave packets encourages studying microscopic fractionalization processes including neutral modes and heat generation, which can be used to identify the appropriate effective model^{34–36,49}. The deterministic fractionalization processes may benefit the search for non-trivial anyonic statistics of fractional charges^{48,50–53}.

Methods

Device fabrication. The devices were fabricated from a standard GaAs/AlGaAs heterostructure with a two-dimensional electron gas (2DEG) located 100 nm below the surface having an electron density of $1.85 \times 10^{11} \text{ cm}^{-2}$ in the dark and $2.07 \times 10^{11} \text{ cm}^{-2}$ after light irradiation at low temperature. After patterning holes into the 2DEG for the Corbino geometry, ohmic contacts were formed by alloying Au–Ge–Ni metal films; subsequently metal gates were patterned using photolithography and electron-beam lithography (see Supplementary Note 1 for details).

Time-of-flight experiment. A charge wave packet was generated by depleting electrons near the injection gate G_1 of length $l_1 \sim 50$ μm by applying a voltage stage $\Delta V_1 = 5\text{--}15$ mV to the static voltage of $-0.2\text{--}0.3$ V. This induced charge $q_1 \sim C_1 l_1 \Delta V_1$ in the packet, where $C_1 l_1$ is the coupling capacitance. The charge waveform $\rho(t)$ was evaluated by applying a detector pulse $\Delta V_D = 20$ mV to the static voltage of

−0.3–−0.4 V on gate G_D to change the transmission probability to the detector ohmic contact by $\Delta T_D \sim 0.17$. This induced a detector current $I_D = \Delta T_D p(t) t_w / T_{\text{rep}}$ with repetition time T_{rep} of the voltage step and the pulse of a width $t_w = 0.08$ – 0.15 ns. The charge in the wave packet was estimated from the integrated current. The time origin of the delay t_d was calibrated from a similar experiment at zero magnetic field, where the wave packet propagates much faster with a velocity on the order of 10^7 m/s^{16,26,38}.

The charge velocity was estimated from the time-of-flight. For the wave packets shown in Fig. 2b, velocities $v_{2/3,u}$ and $v_{1,u}$ of the $\Delta v = 2/3$ and 1 channels under the gate (length L) were estimated from the time-of-flight of the first wave packet in traces (i) and (ii), respectively, by disregarding the short time-of-flight (~ 0.5 ns) in the $\Delta v = 2/3$ ungated channel³⁹. Subsequently, the velocity $v_{1/3,s}$ of the $\Delta v = 1/3$ channel along the side of the gate (length $L + 2\ell$) was estimated from the delay of the second wave packet in trace (ii) and the predetermined $v_{1,u}$. Because the velocity depends strongly on the electrostatic environment, the channels formed along the side of the gates were compared, as shown in Fig. 4d.

Capacitance of interface channel. The interface channel is a compressible stripe of finite width w between two incompressible regions. As the electrostatic potential for this situation is challenging⁵⁴, we assumed finite widths w_g and w_u in the gated and ungated regions, respectively, as shown in Fig. 4a. By considering the incompressible regions as insulators, the capacitance between the channel and the gate was calculated using commercial software COMSOL based on the finite-element method.

Fractionalization factor at high frequencies. We used the plasmon scattering approach to simulate the fractionalization process in the presence of disorder-induced tunneling^{4,46,47}. Consider two one-dimensional chiral channels ($n = 1$ and 2) with conductance σ_n (positive for right movers and negative for left movers), as shown in Fig. 5a. The charge density ρ_n , electrochemical potential V_n , and current $I_n = \sigma_n V_n$ are related to each other with the Coulomb interaction characterized by the self-capacitance C_n (to the ground) and coupling capacitance C_x per unit length^{16,26}. The quantum capacitance was absorbed in those capacitances. Scattering between the channels was considered with scattering conductance g per unit length⁴⁷. Based on current conservation, we derived the following wave equation:

$$-\frac{\partial}{\partial x} \begin{pmatrix} I_1 \\ I_2 \end{pmatrix} = \left[\begin{pmatrix} C_1 + C_x & -C_x \\ -C_x & C_2 + C_x \end{pmatrix} \frac{\partial}{\partial t} + g \begin{pmatrix} 1 & -1 \\ -1 & 1 \end{pmatrix} \right] \begin{pmatrix} V_1 \\ V_2 \end{pmatrix}. \quad (1)$$

Transport eigenmodes $\hat{I}_m = \begin{pmatrix} \tilde{I}_1 \\ \tilde{I}_2 \end{pmatrix}$ can be calculated for alternating current $I_n = \tilde{I}_n e^{i(kx - \omega t)}$ with amplitude \tilde{I}_n at frequency ω . The resulting k (complex) for each mode measures the wavenumber in the real part and the decay rate in the imaginary part. For the fractional case with $\sigma_1 = e^2/h$, $\sigma_2 = -e^2/3h$, and $g > 0$, pure charge and neutral modes with $\tilde{I}_2/\tilde{I}_1 = -1/3$ and -1 , respectively, appeared at $g \gg \omega(C_1 + 3C_2)$ in the disorder-dominated regime, and interaction-dependent modes appeared at $g \ll \omega(C_1 + 3C_2)$ in the interaction-dominated regime. Because the solution in the zero-frequency limit ($\omega \rightarrow 0$) provides the equilibration length $l_{\text{eq}} = \sigma_q/2g$, the disorder-dominated regime corresponds to the plasmon wavelength λ much longer than l_{eq} . Our wave packet contains a long wavelength in the Fourier components ($\lambda \gtrsim 800$ μm in the $\Delta v = 2/3$ channel for the data in Fig. 2b and $\lambda \gtrsim 300$ μm in the $\Delta v = 2$ channel for the data in Fig. 2c). Hence, all data shown herein are obtained from the disorder-dominated regime for our sample with $l_{\text{eq}} \sim 10$ μm . In this case, the charge mode exhibits a slight decay with an angle $\arg[k] \sim 2\pi \left(\frac{C_1 + 3C_2}{C_1 + C_2} \right)^2 \frac{l_{\text{eq}}}{\lambda}$ in the lowest order. This broadens the wave packet only slightly. The time evolutions of I_1 and I_2 in Fig. 5 were obtained by integrating Eq. (1) with current conservation at the boundaries of non-interacting ($C_x = 0$ and $g = 0$) and interacting regions.

Data availability

The data and analysis used in this work are available from the corresponding author upon reasonable request.

Code availability

The codes that are used to generate results in the paper are available from the corresponding author upon reasonable request.

Received: 10 July 2020; Accepted: 2 December 2020;

Published online: 07 January 2021

References

- Giamarchi, T. *Quantum Physics in One Dimension* (Oxford Univ. Press, 2004).
- Safi, I. & Schulz, H. J. Transport in an inhomogeneous interacting one-dimensional system. *Phys. Rev. B* **52**, R17040(R) (1995).
- Ponomarenko, V. V. Frequency dependences in transport through a Tomonaga-Luttinger liquid wire. *Phys. Rev. B* **54**, 10328 (1996).
- Safi, I. A dynamic scattering approach for a gated interacting wire. *Eur. Phys. J. B* **12**, 451 (1999).
- Safi, I. & Schulz, H. J. Interacting electrons with spin in a one-dimensional dirty wire connected to leads. *Phys. Rev. B* **59**, 3040 (1999).
- Gutman, D. B., Gefen, Y. & Mirlin, A. D. Bosonization of one-dimensional fermions out of equilibrium. *Phys. Rev. B* **81**, 085436 (2010).
- Bockrath, M. et al. Luttinger-liquid behaviour in carbon nanotubes. *Nature* **397**, 598 (1999).
- Auslaender, O. M. et al. Tunneling spectroscopy of the elementary excitations in a one-dimensional wire. *Science* **295**, 825 (2002).
- Ishii, H. et al. Direct observation of Tomonaga-Luttinger-liquid state in carbon nanotubes at low temperatures. *Nature* **426**, 540 (2003).
- Chang, A. M. Chiral Luttinger liquids at the fractional quantum Hall edge. *Rev. Mod. Phys.* **75**, 1449 (2003).
- Ezawa, Z.F. *Quantum Hall Effects: Recent Theoretical and Experimental Developments*, 3rd edition. (World Scientific, Singapore, 2013).
- MacDonald, A. H. Edge states in the fractional-quantum-Hall effect regime. *Phys. Rev. Lett.* **64**, 220 (1990).
- Wen, X. G. Electrodynamical properties of gapless edge excitations in the fractional quantum Hall states. *Phys. Rev. Lett.* **64**, 2206 (1990).
- Kane, C. L. & Fisher, M. P. A. Contacts and edge-state equilibration in the fractional quantum Hall effect. *Phys. Rev. B* **52**, 17393 (1995).
- Altimiras, C. et al. Non-equilibrium edge-channel spectroscopy in the integer quantum Hall regime. *Nat. Phys.* **6**, 34 (2010).
- Kamata, H., Kumada, N., Hashisaka, M., Muraki, K. & Fujisawa, T. Fractionalized wave packets from an artificial Tomonaga-Luttinger liquid. *Nat. Nanotech.* **9**, 177 (2014).
- Washio, K. et al. Long-lived binary tunneling spectrum in the quantum Hall Tomonaga-Luttinger liquid. *Phys. Rev. B* **93**, 075304 (2016).
- Sivre, E. et al. Heat Coulomb blockade of one ballistic channel. *Nat. Phys.* **14**, 145 (2017).
- Berg, E., Oreg, Y., Kim, E. A. & Oppen, V. Fractional charges on an integer quantum Hall edge. *Phys. Rev. Lett.* **102**, 236402 (2009).
- le Sueur, H. et al. Energy relaxation in the integer quantum Hall regime. *Phys. Rev. Lett.* **105**, 056803 (2010).
- Itoh, K. et al. Signatures of a nonthermal metastable state in copropagating quantum Hall edge channels. *Phys. Rev. Lett.* **120**, 197701 (2018).
- Levkivskiy, Ivan P. & Sukhorukov, Eugene V. Dephasing in the electronic Mach-Zehnder interferometer at filling factor $\nu = 2$. *Phys. Rev. B* **78**, 045322 (2008).
- Levkivskiy, Ivan P. & Sukhorukov, Eugene V. Noise-induced phase transition in the electronic Mach-Zehnder interferometer. *Phys. Rev. Lett.* **103**, 036801 (2009).
- Grenier, C. et al. Fractionalization of minimal excitations in integer quantum Hall edge channels. *Phys. Rev. B* **88**, 085302 (2013).
- Bocquillon, E. et al. Separation of neutral and charge modes in one-dimensional chiral edge channels. *Nat. Commun.* **4**, 1839 (2013).
- Hashisaka, M., Hiya, N., Akiho, T., Muraki, K. & Fujisawa, T. Waveform measurement of charge- and spin-density wavepackets in a chiral Tomonaga-Luttinger liquid. *Nat. Phys.* **13**, 559 (2017).
- Inoue, H. et al. Charge fractionalization in the integer quantum Hall effect. *Phys. Rev. Lett.* **112**, 166801 (2014).
- Bid, A., Ofek, N., Heiblum, M., Umansky, V. & Mahalu, D. Shot noise and charge at the $2/3$ composite fractional quantum Hall state. *Phys. Rev. Lett.* **103**, 236802 (2009).
- Sabo, R. et al. Edge reconstruction in fractional quantum Hall states. *Nat. Phys.* **13**, 491 (2017).
- Venkatchalam, V., Hart, S., Pfeiffer, L., West, K. & Yacoby, A. Local thermometry of neutral modes on the quantum Hall edge. *Nat. Phys.* **8**, 676 (2012).
- Fabien, L., Rosenblatt, A., Heiblum, M. & Umansky, V. Counter-propagating charge transport in the quantum Hall effect regime. *Science* **363**, 54 (2019).
- Grivnin, A. et al. Non-equilibrated counter-propagating edge modes in the fractional quantum Hall regime. *Phys. Rev. Lett.* **113**, 266803 (2014).
- Lin, C. J. et al. Charge equilibration in integer and fractional quantum Hall edge channels in a generalized Hall-bar device. *Phys. Rev. B* **99**, 195304 (2019).
- Beenakker, C. W. J. Edge channels for the fractional quantum Hall effect. *Phys. Rev. Lett.* **64**, 216 (1990).
- Meir, Y. Composite edge states in the $\nu = 2/3$ fractional quantum Hall regime. *Phys. Rev. Lett.* **72**, 2624 (1994).
- Kane, C. L., Fisher, M. P. A. & Polchinski, J. Randomness at the Edge: theory of quantum Hall transport at filling $\nu = 2/3$. *Phys. Rev. Lett.* **72**, 4129 (1994).
- Protopopov, I. V., Gefen, Y. & Mirlin, A. D. Transport in a disordered $\nu = 2/3$ fractional quantum Hall junction. *Ann. Phys.* **385**, 287 (2017).
- Kamata, H., Ota, T., Muraki, K. & Fujisawa, T. Voltage-controlled group velocity of edge magnetoplasmon in the quantum Hall regime. *Phys. Rev. B* **81**, 085329 (2010).

39. Ashoori, R. C., Stormer, H. L., Pfeiffer, L. N., Baldwin, K. W. & West, K. Edge magnetoplasmons in the time domain. *Phys. Rev. B* **45**, 3894 (1992).
40. Wassermeier, M. et al. Edge magnetoplasmons in the fractional-quantum-Hall-effect regime. *Phys. Rev. B* **41**, 10287(R) (1990).
41. Ernst, G., Zhitenev, N. B., Haug, R. J. & Klitzing, K. von Dynamic excitations of fractional Quantum Hall edge channels. *Phys. Rev. Lett.* **79**, 3748 (1997).
42. Wald, K. R., Kouwenhoven, L. P., McEuen, P. L., van der Vaart, N. C. & Foxon, C. T. Local dynamic nuclear polarization using quantum point contacts. *Phys. Rev. Lett.* **73**, 1011 (1994).
43. Kumada, N., Kamata, H. & Fujisawa, T. Edge magnetoplasmon transport in gated and ungated quantum Hall systems. *Phys. Rev. B* **84**, 045314 (2011).
44. Hashisaka, M. & Fujisawa, T. Tomonaga–Luttinger-liquid nature of edge excitations in integer quantum Hall edge channels. *Rev. Phys.* **3**, 32 (2018).
45. Nakamura, J. et al. Aharonov–Bohm interference of fractional quantum Hall edge modes. *Nat. Phys.* **15**, 563 (2019).
46. Hashisaka, M., Washio, K., Kamata, H., Muraki, K. & Fujisawa, T. Distributed electrochemical capacitance evidenced in high-frequency admittance measurements on a quantum Hall device. *Phys. Rev. B* **85**, 155424 (2012).
47. Nosiglia, C., Park, J., Rosenow, B. & Gefen, Y. Incoherent transport on the $\nu = 2/3$ quantum Hall edge. *Phys. Rev. B* **98**, 115408 (2018).
48. Spånslätt, C., Park, J., Gefen, Y. & Mirlin, A. D. Topological classification of shot noise on fractional quantum Hall edges. *Phys. Rev. Lett.* **123**, 137701 (2019).
49. Wang, J., Meir, Y. & Gefen, Y. Edge reconstruction in the $\nu = 2/3$ fractional quantum Hall state. *Phys. Rev. Lett.* **111**, 246803 (2013).
50. Halperin, B. I. Statistics of quasiparticles and the hierarchy of fractional quantized Hall states. *Phys. Rev. Lett.* **52**, 1583 (1984).
51. Nayak, C., Simon, S. H., Stern, A., Freedman, M. & Sarma, S. D. Non-Abelian anyons and topological quantum computation. *Rev. Mod. Phys.* **80**, 1083 (2008).
52. Bartolomei, H. et al. Fractional statistics in anyon collisions. *Science* **368**, 173 (2020).
53. Nakamura, J., Liang, S., Gardner, G. C. & Manfra, M. J. Direct observation of anyonic braiding statistics. *Nat. Phys.* **16**, 931 (2020).
54. Khaetskii, A. V., Fal'ko, V. I. & Bauer, G. E. W. Electrostatics of inter-Landau-level diodes. *Phys. Rev. B* **50**, 4571 (1994).

Acknowledgements

The authors thank T. Hata and Y. Tokura for their beneficial discussions. This study was supported by the Grants-in-Aid for Scientific Research (JP15H05854, JP19H05603) and

the Nanotechnology Platform Program of the Ministry of Education, Culture, Sports, Science and Technology, Japan.

Author contributions

T.F. designed and supervised this study. C.L. fabricated the device and performed the experiment with help from M.H. and T.F. T.A. and K.M. grew the wafer. C.L. and T.F. analyzed the data and wrote the manuscript. All authors discussed the results and commented on the manuscript.

Competing interests

The authors declare no competing interests.

Additional information

Supplementary information is available for this paper at <https://doi.org/10.1038/s41467-020-20395-7>.

Correspondence and requests for materials should be addressed to C.L. or T.F.

Peer review information *Nature Communications* thanks the anonymous reviewers for their contribution to the peer review of this work.

Reprints and permission information is available at <http://www.nature.com/reprints>

Publisher's note Springer Nature remains neutral with regard to jurisdictional claims in published maps and institutional affiliations.



Open Access This article is licensed under a Creative Commons Attribution 4.0 International License, which permits use, sharing, adaptation, distribution and reproduction in any medium or format, as long as you give appropriate credit to the original author(s) and the source, provide a link to the Creative Commons license, and indicate if changes were made. The images or other third party material in this article are included in the article's Creative Commons license, unless indicated otherwise in a credit line to the material. If material is not included in the article's Creative Commons license and your intended use is not permitted by statutory regulation or exceeds the permitted use, you will need to obtain permission directly from the copyright holder. To view a copy of this license, visit <http://creativecommons.org/licenses/by/4.0/>.

© The Author(s) 2021